Regularized ultrasound phantom-free local attenuation coefficient slope (ACS) imaging in homogeneous and heterogeneous tissues

Iman Rafati, François Destrempes, Ladan Yazdani, Marc Gesnik, An Tang, Guy Cloutier, *Senior Member, IEEE*

***Abstract*— Attenuation map or measurements based on local attenuation coefficient slope (ACS) in quantitative ultrasound (QUS) has shown potential for diagnosis of liver steatosis. In liver cancers, tissue abnormalities and tumors detected using ACS are also of interest to provide new image contrast to clinicians. Current phantom-based approaches have the limitation of assuming comparable speed of sound between the reference phantom and insonified tissues. Moreover, these methods present the inconvenience for operators to acquire data on phantoms as well as on patients. The main goal was to alleviate these drawbacks by proposing a methodology for constructing phantom-free regularized (PF-R) local ACS maps and investigate the performance in both homogeneous and heterogeneous media. The proposed method was tested on two tissue mimicking media with different ACS constructed as homogeneous phantoms, side-by-side and top-to-bottom phantoms, and inclusion phantoms with different attenuations. Moreover, an *in-vivo* proof-of-concept was performed on healthy, steatotic and cancerous human liver datasets. Modifications brought to previous works include: a) a linear interpolation of the power spectrum in log-scale; b) the relaxation of the underlying hypothesis on the diffraction factor; c) a generalization to nonhomogeneous local ACS; and d) an adaptive restriction of frequencies to a more reliable range than the usable frequency range. Regularization was formulated as a generalized LASSO, and a variant of the Bayesian Information Criterion (BIC) was applied to estimate the Lagrangian multiplier on the LASSO constraint. In addition, we evaluated the proposed algorithm when applying median filtering before and after regularization. Tests conducted showed that the PF-R yielded robust results in all tested conditions, suggesting potential for additional validation as a diagnosis method.**

***Index Terms*— Compression wave attenuation imaging, local attenuation coefficient slope, quantitative ultrasound, regularization, system independent tissue characterization, ultrasound attenuation coefficient estimation.**

I. Introduction

HEPATOCELLULAR carcinoma (HCC) is responsible for between 85% and 90% of primary liver cancers [1, 2], and they are the fourth most common cause of cancer-related mortality [3]. The mortality rate of HCC is increasing 3% per year due to late diagnosis [4, 5]. Early detection of HCC is critical to increase the opportunity for curative treatment and to improve survival. Ultrasound (US) is used clinically for HCC surveillance due to its wide availability, cost-effectiveness and noninvasiveness compared to other methods such as biopsy, magnetic resonance imaging (MRI) and computed tomography [6, 7]. However, US has a lower sensitivity [8, 9] for detecting focal lesions, especially in the presence of concomitant liver steatosis, fibrosis, or cirrhosis [10, 11]. To overcome this limitation, one may extract additional information from US not available on B-mode, Doppler, or elastography images, such as attenuation coefficient slope (ACS) maps estimated using quantitative ultrasound (QUS) [12-15].

QUS attenuation has been used in several clinical studies to assess the degree of liver injury and specifically of liver steatosis [16-19]. This feature is used by radiologists to detect and assess the severity of fatty liver disease. The accumulation of fat in liver can progress to fibrosis, cirrhosis, and eventually to HCC [20]. The presence of moderate-to-severe liver steatosis constitutes a diagnostic challenge as it may obscure tumors in attenuated portions of the liver [21]. US attenuation is more economical than MRI for screening and surveillance [22], mainly due to clinical successes of the controlled attenuation parameter (CAP) to grade liver steatosis [17]. Notice that no images are produced with the CAP parameter.

The loss of ultrasonic energy when an acoustic wave propagates through soft tissues is referred to as ultrasonic attenuation [23]; it is due to scattering and absorption (conversion of ultrasonic to thermal energy) [24]. Clinicians performing conventional B-mode assessment can detect attenuation qualitatively [25, 26]. The attenuation is related to the interaction of propagating compression waves within tissues, resulting in a decrease in the echo intensity along the wave propagation path, loss in B-mode detectable image features, and shadowing [27]. While attenuation was traditionally considered as an imaging artifact, it can be leveraged as a specific feature with diagnostic value [12]. Indeed, attenuation depends on the underlying nature and structure of a tissue [28]. To clarify this concept, several parameters can be defined as attenuation in the US literature. The total attenuation coefficient (total AC) is defined as the attenuation-to-depth ratio, which depends on intervening tissues along the whole propagation path [12, 23]. The local AC can be defined as the partial derivative of attenuation with respect to depth, which depends on tissues at a given position [29]. By assuming a linear dependency on frequency, the slope of AC (attenuation coefficient slope - ACS) is most often used in the literature [23, 25, 30-35].

Constructing attenuation images is an approach that can be used to assist the detection of lesions and abnormalities of the liver. Popular methods to estimate ACS using clinical US scanners in backscattering mode [15, 36, 37] are the spectral difference [38, 39] and spectral shift [40] methods. Both spectral-based approaches estimate the local ACS (dB cm^{-1} MHz^{-1}) inside a pre-specified region-of-interest (ROI) [23]. The spectral difference method uses the reduction of the echo signal

power with depth to determine the local attenuation coefficient, whereas the spectral shift method utilizes the downshift in the center frequency of the backscatter echo with depth to obtain frequency-dependent attenuation [15, 40]. The spectral log-difference method [23, 34] and a hybrid method [32] are two other variants of these techniques.

With these methods, scattering properties (*i.e.*, the backscatter coefficient) are assumed to be constant over depth within the ROI. Furthermore, to compensate for the US beam diffraction and other system-dependent effects, such as gain, filtering, and the piezoelectric acoustical transfer function at emission and reception, echo signals from a reference phantom whose acoustic properties are known (through calibration) is required [41]. It is worth mentioning that these echo signals must be acquired using the same equipment and system settings as the clinical exam, and that the speed of sound of the reference phantom needs to be close to the one of acquired tissues' samples [12, 23]. The ratio of power spectra from tissues' samples and reference phantom, at two different depths, yields the local attenuation coefficient of the scanned organ at the frequency and depth of interest [14]. The availability of a well-calibrated reference phantom can thus be considered as a limitation of these methods [42].

Recent studies proposed system independent methods as an alternative for estimating local attenuation without the need of a reference phantom [42, 43]. This strategy cancels system dependent effects using spectral normalization in adjacent frequency components and is known as the reference frequency method (RFM). This method has some limitations such as the need of a pre-defined frequency range and of a large computing window (a square with side lengths of 2.5 cm), which make the use of this method limited to the case of homogeneous media preventing cancer lesions detection. Thus, a method is needed to overcome these limitations to provide parametric maps for cancer diagnosis purposes. In our preliminary study [43], reconstructions of attenuation images using a system independent method showed promising results close to the ground truth (through-transmission substitution method) [36], in the case of homogeneous and side-by-side phantoms. The current study provides additional validations with top-to-bottom phantoms, and is also focusing on differentiating lesions with different attenuation and geometrical properties than surrounding tissues. More specifically, we present the development and validation of a phantom-free attenuation mapping method with parametric regularization to reduce image artifacts for applications in liver steatosis grading, and liver cancer detection and characterization.

The remaining part of this paper is organized as follows. Section II introduces the theoretical framework and governing equations for estimating the attenuation coefficient slope (ACS). Section III describes experimental configurations and acquisitions. Section IV presents results acquired on phantoms with the phantom free (PF) and the spectral log-difference (SLD) methods before and after regularization (R). Section V discusses advantages and future directions, followed by Section VI on conclusions.

II. Theoretical framework

The ACS can be evaluated using a methodology that involves radiofrequency (RF) data acquisition without the need of acquiring RF signals from a reference phantom. The method is based on spectra normalization at different frequencies [43]. Specific contributions are: 1) a linear interpolation of the power spectrum in log-scale; 2) the relaxation of the underlying hypothesis on the diffraction factor within an ROI; and 3) a generalization to nonhomogeneous local ACS. Moreover, we provide a regularized local attenuation map based on the selected ROI.

A. Power spectrum modeling

Within the ROI, a computing window (CW) centered at depth z (cm) (the lateral position is dropped in the equations for simplicity of notation) is considered. The power spectrum $S(f,z)$ at depth z of backscattered RF signals in the time domain ($x_z(t)$) after removing the time gain compensation (TGC) of the US system, which was automatically recorded as a function of depth, can be computed as in Eq. (1):

$$S(f,z) = \left\langle \left| X_z(f) \right|^2 \right\rangle \quad (1)$$

where f (MHz) is the frequency, $X_z(f)$ is the Fourier transform of $x_z(t)$ over a scan line centered at z, $|X_z(f)|$ denotes the complex modulus of $X_z(f)$ and $\langle - \rangle$ represents the averaging operator over scan lines. Power spectra were estimated by computing Fourier transforms of RF signals after applying a rectangular window with zero padding, and averaging over 25 adjacent scan lines (see [44]).

The power spectrum can be modeled as a function of the US frequency and depth according to previous studies [31, 42], in the form of the following equation:

$$S(f_i,z_k) = G(f_i)D(f_i,z_k)BSC(f_i,z_k)A(f_i,z_k), \quad (2)$$

where S is the power spectrum as a function of frequency f_i (i is the frequency component index) and depth z_k (k is the depth index), G is the transducer's response in transmit and receive modes at a given frequency, D represents combined effects of focusing, beamforming, and beam diffraction, BSC ($cm^{-1}.\ sr^{-1}$) is the backscatter coefficient, and A is the attenuation component, which is assumed to be in the form $\exp(-4\alpha_{total,z_k} z_k f_i)$, where α_{total,z_k} (Nepers cm^{-1} MHz^{-1}) is the total ACS at depth z_k, assuming a linear dependency with frequency.

The first modification to [43] was to consider a Gaussian fit in log-scale to power spectra for improving robustness of ACS maps. Next, according to [42], the power ratio $RS(f_i,z_k)$ (no unit) between adjacent frequency components $S(f_i,z_k)$ and $S(f_{i-1},z_k)$ can be expressed as:

$$RS(f_i,z_k) = \frac{S(f_i,z_k)}{S(f_{i-1},z_k)} =$$

$$\frac{G(f_i)D(f_i,z_k)BSC(f_i,z_k)A(f_i,z_k)}{G(f_{i-1})D(f_{i-1},z_k)BSC(f_{i-1},z_k)A(f_{i-1},z_k)}. \quad (3)$$

We assume that beamforming and diffraction effects between two adjacent frequencies f_i and f_{i-1} are related linearly in the form $D(f_i,z_k)=c_iD(f_{i-1},z_k)$, where the unknown constant of proportionality c_i depends only on frequencies f_i and f_{i-1}. With this assumption, Eq. (3) simplifies to:

$$RS(f_i,z_k)=\frac{G(f_i)c_iBSC(f_i,z_k)A(f_i,z_k)}{G(f_{i-1})BSC(f_{i-1},z_k)A(f_{i-1},z_k)}. \quad (4)$$

To obtain a linear equation, the natural logarithm is applied to Eq. (4) yielding:

$$\log RS(f_i,z_k)=\log G(f_i)-\log G(f_{i-1})+\log BSC(f_i,z_k) -\log BSC(f_{i-1},z_k)-4\alpha_{total,z_k}z_k(f_i-f_{i-1})+\log c_i. \quad (5)$$

By taking the difference in the expression $\log RS(f_i,z_k)$ at two different depths z_k and z_r yet at same frequencies, the terms for transmit and receive transducer's responses and the backscatter coefficient can be cancelled from Eq. (5) by assuming $BSC(f_i,z_k)=BSC(f_i,z_r)$. Furthermore, upon considering the relation $\alpha_{total,z_k}z_k=\alpha_{total,z_r}z_r+\alpha_{local,z}(z_k-z_r)$, where $\alpha_{local,z}$ is the local ACS for a CW centered at depth z, Eq. (5) yields after simplifications:

$$\log RS(f_i,z_k)-\log RS(f_i,z_r)=-4\alpha_{local,z}(z_k-z_r)(f_i-f_{i-1}). \quad (6)$$

To lighten notation in Eq. (6), the normalized ratio of power spectra $RS_{nor}(f_i,z_k,z_r)$ is defined as:

$$RS_{nor}(f_i,z_k,z_r)=RS(f_i,z_k)/RS(f_i,z_r). \quad (7)$$

With this definition, Eq. (6) now reads as:

$$\log RS_{nor}(f_i,z_k,z_r)=-4\alpha_{local,z}(z_k-z_r)(f_i-f_{i-1}). \quad (8)$$

Another modification to Gong *et al.* [42] was restricting the frequency range within the usable frequency range (UFR) as follows. First, the log-power spectrum ratio at a given frequency f as a function of depth z was approximated by a linear function $-a(f)z+b(f)$ using the line fitting described in Section II.B. The frequency f_* at which the y-intercept $b(f)$ is maximal was selected. This procedure yielded the frequency with overall maximal power spectrum. The quantity $a(f_*)$ represents an approximate estimate of the local ACS at frequency f_*; see Eq. (2). The frequency range was then restricted to those frequencies f_i for which the ratio (obtained from Eq. (8)) lies within 25% of $a(f_*)$:

$$(1-0.25)a(f_*)\le\frac{\log RS_{nor}(f_i,z_k,z_r)}{-4(z_k-z_r)(f_i-f_{i-1})}\le(1+0.25)a(f_*) \quad (9)$$

The final local ACS estimate was obtained by performing a linear regression on Eq. (8) within the obtained restricted frequency range, which is ROI-dependent. Based on data inspection, the frequency range turned out to be continuous. This is a new alternative to the procedure that was proposed by Gong *et al.* [42], where the frequency range was selected by considering the top of the histogram of the estimated parameter. The new method was applied to small CWs within the ROI to obtain a local ACS map, as shown in Fig. 1. In this illustrative example of an arbitrary ROI, height and width of CWs were approximately 8 mm (10 pulse lengths) by 7 mm (25 scan lines), respectively, with 70% and 75% overlapping in lateral and axial directions, respectively. These window dimensions and overlaps remained constant for all results presented in this study.

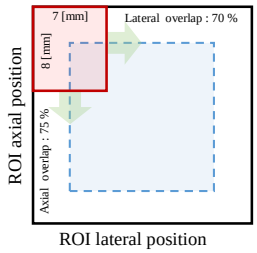

Fig. 1. Schematic of a ROI (black box); one computing window (CW) (red box); and center positions of CWs included into the blue box in dashed line. Overlaps of CWs in lateral and axial positions are 70% and 75%, respectively.

B. Line fitting method

The purpose of this method is to find a linear relation between the depth (z) and the logarithm of power spectra ratio ($\log RS$). Under the random sample consensus (RANSAC) approach, outlier values (*i.e.*, points too far away from the regression line) in experimental data are being removed from the line fitting [45]. A second issue is the boundary between two different media in the tissues' samples. In presence of two media, there might be two lines with different slopes. It should be mentioned that points used for the line-fitting method are denoted as inliers in the RANSAC approach. The following algorithm, displayed in Fig. 2, was used to find the slope based on the number of points per line (inliers), after outliers' rejection.

In Fig. 2 (a), we considered three possible cases to find inliers. In the first case, there is no change in slope's sign among fitted lines through consecutive depths (z_k). If there is a single slope, which represents the case of a homogenous sample with a single medium, then all points are considered for line-fitting. If there are two different slopes, but with same sign (second case), we assume a piecewise linear curve consisting of two segments. We chose the largest slope in absolute value, *i.e.* $\arg\max\ abs\{(\log RS(i+1)-\log RS(i))/(z(i+1)-z(i))\}$, to determine the location of the change in segments. Inliers are then the points belonging to the segment comprising the most points. In case of tie, the first segment was selected as set of inliers. In the third case, there is a change in slope's sign among fitted lines through consecutive depths. As in the second case, inliers are then the points of the segment comprising the most points (taking the segment occurring first in case of tie).

In Fig. 2 (b), RANSAC line fitting was applied to selected inliers, as in [45, 46]. Two modifications were brought to RANSAC original formulation. The first one is to examine all

combinations of two points instead of selecting randomly two points, which is convenient due to the limited number of points in this context (less than 10 points based on the size of segments, see Fig. 2). As for the second modification, instead of considering an acceptable number of inliers based on a fixed threshold and choosing a pair of points with maximal number of inliers, the selection of pairs of points was based on both the number of inliers and the proximity of other points to the fitted line, using no fixed threshold. Therefore, all combinations of two points (*i* and *j*) among inliers were being considered. An initial threshold (T_{new}) was set such that half of the remaining points were within the threshold. As a result, at least half of the points (including the pair that defined the line) has been considered as inliers. This threshold was updated by iterations on all combinations of two points (*M* in Fig. 2(b)). Finally, the line with the lowest threshold that contained more than half of points was selected as the result of the line fitting.

C. Regularization

1. Linear regression formulation and data fidelity term

In the context of regularization of parametric maps in which each pixel represents a CW, a linear regression formulation of the following form can be defined:

$$y_r = X_r \beta_r + \varepsilon_r \tag{10}$$

where r denotes a CW, $y_r = (y_r(f_i))_{i=1}^{N_{Freq}}$ represents the observed spectral data expressed at each frequency f_i (MHz) of the discretized UFR. Moreover, the matrix X_r represents the model's predictors, while β_r corresponds to the vector of regression coefficients. Here, ε_r is the residual noise, assumed to be zero-mean with variance σ^2. Assuming independent identically distributed residual noise over all CWs, one is led to the following data fidelity term (*i.e.*, the residual "res", which expresses the least mean squared error (LMSE) between the observed data and the fitted model):

$$\mathrm{res}(y,\beta) = \frac{1}{2}\sum_{r=1}^{N_{CW}} w_r^2 \left\| y_r - X_r \beta_r \right\|_2^2, \tag{11}$$

where N_{CW} is the number of CWs for parameters estimation, w_r is a positive weight assigned to the CW indexed by *r*, and $\|-\|_2$ denotes the ℓ_2-norm. The likelihood $\mathcal{L}(y \mid \beta, \sigma^2)$ is then of the form: $\exp(-\mathrm{res}(y,\beta)/\sigma^2)$.

The data fidelity term is detailed as follows in the case of the proposed phantom-free local attenuation model, whilst this term in the case of the SLD model used for comparison is described in Appendix. The observed spectral data is the left-hand side of Eq. (8) and is then given by (viewed as a vector):

$$y_r = (\log RS_{nor}(f_i, z_k, z_k))_{i=1}^{N_{Freq}}. \tag{12a}$$

The predictors' matrix (a vector in this case) and the regression coefficient (a scalar in this case) are then of the form:

$$X_r = (-4(z_k - z_n)(f_i - f_{i-1}))_{i=1}^{N_{Freq}}, \text{ and} \tag{12b}$$

$$\beta_r = \alpha_{r,local}. \tag{12c}$$

To determine the weights w_r appearing in Eq. (11), we first solved this LMSE problem with initial weights set to 1. Then, Fisher tests [47] were applied to each underlying linear regressions and the resulting *p*-values were adopted as weights in that equation. In case of a numerically vanishing *p*-value, it was replaced by the small quantity 10^{-5}.

2. Regularization term

In LASSO framework, the ℓ_1-norm regularization term imposed on linear regression coefficients β is of the form [48]:

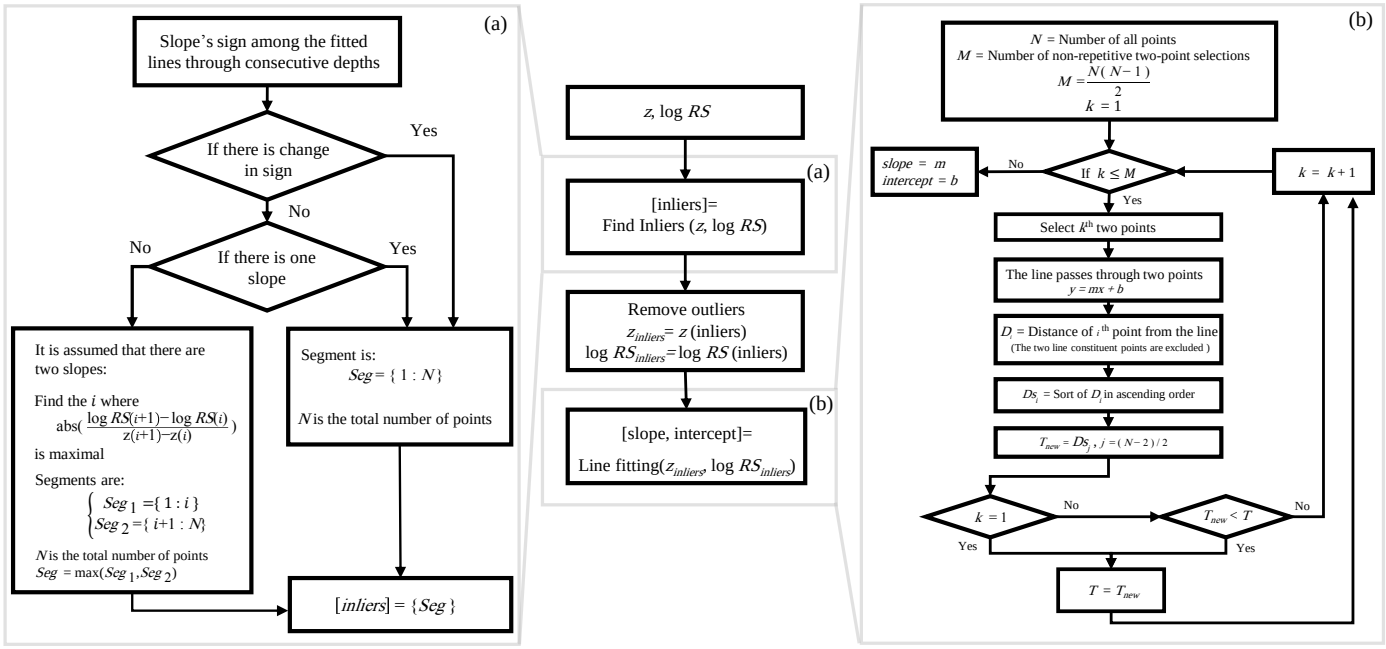

Fig. 2. Algorithm for approximate estimation of the local ACS at a given frequency, by line fitting the logarithm of power spectra ratio (log RS) at a given frequency as a function of depth *z*. (a) The algorithm consists of finding inliers (*i.e.*, the points to be considered for line fitting), and (b) the slope of the fitted line on the inliers based on a RANSAC approach.

$$\mathrm{reg}_1(\beta,\lambda)=\lambda\sum_{r=1}^{N_{CW}}\sum_{m=1}^{d}\sum_{s\in N(r)}\left|\beta_{r,m}-\beta_{s,m}\right|, \qquad (13a)$$

where λ is the Lagrange multiplier (LM), which weights the strength of the constraint with respect to the data fidelity term, $d=1$ for the phantom-free attenuation method or $d=2$ for the SLD attenuation model (see Appendix A), where d is the number of model parameters being estimated, and $N(r)$ denotes the set of previous (adjacent) CWs to a given CW, one along the axial direction, the other along the lateral direction. This constraint favors naturally identical regression coefficients on adjacent CWs, and hence causes CWs to get fused (*i.e.*, to share the same regression coefficients). In the LASSO formalism, Eq. (8) may be recast in the form:

$$\mathrm{reg}_1(\beta,\lambda)=\lambda\left\|D\beta\right\|_1, \qquad (13b)$$

where D represents the constraint matrix, $\beta=(\beta_r)$ is the vector of regression coefficients, and $\|-\|_1$ denotes the ℓ_1 -norm. However, to address adjacent CWs belonging to different tissues, the links between adjacent CWs were assessed based on Nakagami goodness-of-fit tests along axial and lateral directions. Namely, the Kolmogorov-Smirnov goodness-of-fit test [49] was applied to the data corresponding to the US echo envelope encompassing the two adjacent CWs, with Nakagami distribution [50] as the underlying statistical model. When the goodness-of-fit failed between two adjacent CWs (with a confidence level of 0.1), the corresponding link was removed in the constraint matrix D (*i.e.*, the corresponding entry was set to 0).

The corresponding prior on regression coefficients is of the form: $\pi(\beta\,|\,\lambda)=\exp(-\mathrm{reg}_1(\beta,\lambda))$. For a given LM value λ, one seeks the vector of coefficients $\hat{\beta}(\lambda)$ that minimizes the corresponding energy functional:

$$\mathrm{res}(y,\beta)+\mathrm{reg}_1(\beta,\lambda). \qquad (14)$$

Notice that in principle the LASSO constraint favors sparsity in differences of regression coefficients, even more so than the ℓ_2 -norm regularization constraint. From Tibshirani and Taylor [48], the curve expressing $\mathrm{res}(y\,\hat{\beta}(\lambda))+\mathrm{reg}(\hat{\beta}(\lambda),\lambda)$ as a function of λ can be described as a piece-wise linear curve, based on finitely many values of λ, which are obtained efficiently with the path algorithm [48]. In the current work, we used our own implementation of the path algorithm on Matlab (version R2018a, The MathWorks, Natick, MA).

3. Model's selection

The Bayesian Information Criterion (BIC) [51] yields in LASSO framework [48] the expression:

$$\mathrm{BIC}(\lambda)=-2\log\mathcal{L}(y\,|\,\hat{\beta}(\lambda),\hat{\sigma}^2)+C(\lambda)\log N, \qquad (15)$$

Where $\mathcal{L}(y\,|\,\beta,\sigma^2)$ represents the likelihood of the data based on parameters β and σ^2, $\hat{\beta}(\lambda)$ are the regression coefficients based on the LM λ, $\hat{\sigma}^2$ is the maximum likelihood estimator of the variance σ^2, $N=\dim(y_r)$ is the total sample size in the linear regression problem, and $C(\lambda)$ is the resulting model's complexity. In this work, $C(\lambda)$ was considered as the degrees of freedom *df* of the solution to Eq. (14) times the number of windows within one CW, *i.e.* the number of depths z_k considered in Eq. (12a), since each coefficient β_r intervenes on these distinct windows, albeit with values already fused to a single one. For the SLD attenuation method (Appendix), $C(\lambda)$ was taken as *df* times 2 (*i.e.*, the number of regression coefficients). Thus, having fixed λ, hence $\hat{\beta}_r(\lambda)$, one obtains under stated hypotheses on the observed spectral data noise:

$$\hat{\sigma}^2=\frac{1}{N}\sum_{r=1}^{N_{CW}}w_r^2\left\|y_r-X_r\hat{\beta}_r(\lambda)\right\|_2^2. \qquad (16)$$

This yields the log-likelihood term for some irrelevant additive constants (*const.*):

$$\begin{aligned}&-2\log\mathcal{L}(y\,|\,\hat{\beta}(\lambda),\hat{\sigma}^2)=\\&N\,\log(2\pi\hat{\sigma}^2)+\frac{1}{\hat{\sigma}^2}\sum_{r=1}^{N_{ROI}}w_r^2\left\|y_r-X_r\hat{\beta}_r(\lambda)\right\|_2^2=\\&N\,\log\mathrm{res}(y,\hat{\beta}(\lambda))+const.\end{aligned} \qquad (17)$$

According to the above equations (Eq. 15 to Eq. 17), the BIC criterion is formulated as choosing the value of λ that minimizes the BIC curve [51]. This is equivalent (as N tends to infinity) to choosing the model (represented here by the fused CWs) for which the data likelihood $\int\mathcal{L}(y\,|\,\beta)\,\pi(\beta\,|\,\lambda)\,d\beta$ is maximal (notice that the larger data likelihood corresponds to the smaller BIC value), where $\pi(\beta\,|\,\lambda)$ denotes the prior on regression coefficients implied by the LM.

To favor a greater number of fused CWs within local attenuation maps, we adopted in this work a "strong BIC" criterion [31, 43], which is defined by selecting the largest value of λ for which the condition $BIC(\lambda)\le BIC(0)$ remains valid. This is equivalent to selecting the model that offers the same likelihood as the model without any regularization, but with as much regularization as allowed under this condition. Thus, the LM was maximized as to yield a BIC value no worse than that of the maximum likelihood.

III. Materials and Methods

A. Phantom experiments description

1. Phantoms fabrication

Two media were made with a mixture of agar (2% (w/w)), glycerol (10%) and graphite powder (mixture #1, 4.5%; mixture #2, 12%) to investigate the performance of ACS methods in the case of homogeneous and heterogeneous samples [52]. Three categories of phantoms with homogeneous, side-by-side and top-to-bottom homogeneous media, and heterogeneous samples with inclusions were made using these two gel preparations.

a) Homogeneous, side-by-side, and top-to-bottom phantoms

Two homogeneous phantoms were made using mixture #1 (model A) and mixture #2 (model B). A side-by-side phantom

(model C) was also made by cutting half of one homogeneous phantom in its mold after jellifying and pouring the other mixture into the mold. The other orientations of model C (top-to-bottom) in which mixture #2 was on top and mixture #1 at the bottom resulted in model D, and vice versa for model E.

b) Heterogeneous phantoms with inclusions

Inclusion phantoms with different characteristics were made into a single container. Three cylindrical molds with diameters of 10, 15 and 20 mm were glued to the bottom of the container. Each cylindrical mold was made of acrylonitrile butadiene styrene (ABS) and was fabricated by 3D-printing (Dimension Elite, Stratasys Inc., Eden Prairie, MN, USA). The mixture #1 was poured in the container with ABS cylindrical molds in it, and molds were removed after jellification. Resulting holes were filled with mixture #2.

2. Data acquisition and post-processing

A Verasonics Vantage 256 scanner (Redmond, WA) equipped with an ATL L7-4 probe (Philips, Bothell, WA) driven at 5 MHz was used to perform US acquisitions. Coherent compounding was done with 21 angles (-10° to 10°) and one hundred frames were acquired for each phantom. The f-k migration method was used for beamforming RF data [53]. To allow comparing results obtained with the proposed PF attenuation method with those of the SLD method using the same LASSO regularization approach, acquisitions with the same settings were made on a reference phantom (117GU-101 CIRS, Norfolk, VA). For the subset of results with inclusion phantoms, a median filter (MF) with a window size 5×5 pixels was applied on PF attenuation images to compare with results using regularization.

3. Gold-standard attenuation measurements

ACS ground truth values (dB cm^{-1} MHz^{-1}) were estimated on pieces of the same phantoms made with mixtures #1 and #2, using a planar reflection method, with the same probe and system settings as for acquisitions on gel samples [36]. A cubic piece of each phantom was put onto a glass reflector in distilled water and attenuation was estimated by measuring the amplitude difference of the US signal reflected by the glass plate, with and without the sample in the path.

B. In-vivo liver data description

Four human liver US datasets were used to test the effectiveness of ACS methods. *In-vivo* data included a healthy liver, a steatotic liver, a liver with a primary HCC, and another with a metastatic cancer. Clinical protocols were approved by the institutional review board of the *Centre hospitalier de l'Université de Montréal*. All recruited participants gave written informed consent.

1. Nonalcoholic fatty liver disease (NAFLD)

Non-alcoholic *in-vivo* human liver datasets with different pathological conditions were investigated in two participants. The magnetic resonance imaging (MRI) proton density fat fraction (PDFF) was used to grade liver steatosis [54, 55]. The Achieva TX 3T MRI system (Philips Healthcare, Best, Netherlands) was used and the protocol consisted in using a two-channel body coil for transmission and a 16-channel surface array coil for signal reception with a 3D chemical-shift encoded multi-echo gradient-echo sequence using 6 echoes (mDixon Quant). The water/fat separation was performed in the complex-domain using a multi-frequency spectral fat model and a T2* correction. A low flip angle was used to avoid T1 bias. The liver biopsy was also available to assess the whole spectrum of the disease. The first participant had a histological steatosis grade of zero (S0) indicating the absence of steatosis. The second patient had a steatosis grade 2 (S2) indicating moderate steatosis.

2. Liver cancers

Two *in-vivo* human liver cancers were studied. The diagnosis was made using MRI as the reference standard. One patient had a circular 15-mm HCC mass, and the other one had one lesion corresponding to a colorectal liver metastasis (oval mass of 20 × 49 mm).

3. Data acquisition and post-processing

The same Verasonics US system as for phantom experiments was used to collect 30 frames of data for each liver using a curvilinear array transducer (ATL C5-2, Philips, Bothell, WA, USA) driven at 3.1 MHz. Coherent compounding was done with 21 angles (-10° to 10°) using the f-k RF data migration [53]. The same probe and system settings were used to acquire US data on a reference phantom for the SLD method.

C. Parameter settings of ACS algorithms

For phantom experiments, all computations were done in the Cartesian domain (*x*-*z*). To compare the performance of the phantom-free regularization approach, the SLD method was implemented according to our previous work [31], and the equations are provided in Appendix. The power spectra of the proposed PF and SLD methods were averaged over 25 scan lines, each spanning 10 pulse lengths on overlapping windows. For *in-vivo* liver datasets, computations were done in the polar domain (r - θ). To compare performance of ACS methods, all parameters were set to the same values as for phantom experiments.

As an extra comparison for homogenous phantoms, the RFM was used with a CW with size equal to 2.5 × 2.5 cm, and within the range of frequency of 4-6 MHz, in accordance with [42]. No attenuation maps were provided for this method because the size of the CW was much larger than for PF and SLD methods.

D. Data analysis

To compare experimental results on phantoms, biases were calculated as the difference of mean values with the ground truth. Also, the normalized root-mean-squared errors (NRMSE) were computed as follows:

$$\mathrm{NRMSE} = \frac{1}{\bar{x}}\sqrt{\frac{\sum_{i=1}^{N}(x_i - \hat{x}_i)^2}{N}}, \qquad (19)$$

where $\bar{x}$ represents the mean attenuation among N datasets, x_i is the ground truth value at the i^{th} position, and $\hat{x}_i$ represents

the estimated value at the same position. For both biases and NRMSEs, standard deviations (SDs) were also calculated.

The contrast-to-noise ratio (CNR) for attenuation coefficient maps in the case of side-by-side, top-to-bottom and inclusion phantoms, and liver cancers was computed as:

$$\mathrm{CNR} = \frac{|\bar{x}_{m1} - \bar{x}_{m2}|}{\sqrt{\sigma_{m1}^2 + \sigma_{m2}^2}}, \qquad (20)$$

where $\bar{x}$ and σ are mean and SD of ACS values within the medium #1 ($m1$) and medium #2 ($m2$), corresponding to both tissues present or expected (*i.e.*, either side-by-side or top-to-bottom media, gel surrounding or within the phantom inclusion, or liver parenchyma versus tumor, respectively).

A one-way analysis of variance (ANOVA) with repeated measures was performed on mean values of the two ACS methods evaluated on phantoms, with the presence or not of regularization as the co-factor. In the case where the Shapiro-Wilk normality test failed, the Friedman test was used as the non-parametric analogue. In these tests, the sample size was 55, including 10 homogeneous phantom acquisitions, 3 side-by-side phantom acquisitions, 6 top-to-bottom phantom acquisitions, and 36 inclusion phantom acquisitions. For CNRs, the sample size of the ANOVA test was 45 (homogenous phantoms were excluded). The Sigmaplot software (version 11.0.0, Systat, Palo Alto, CA) was used to perform statistical analyses.

For *in-vivo* NAFLD data, as there was no ground truth, the comparison of ACS methods with and without regularization was done by comparing mean values and coefficients of variation (CV = SD / mean) within the ROI. For *in-vivo* cancer data, mean values and CNRs were used for comparison. The positions of lesion and background tissues were found by an expert radiologist based on MRI. CNRs for cancer data were computed based on one rectangle within the lesion and two rectangles within the liver parenchyma, on top and bottom of the lesion (see Fig. 8). One can compute a single CNR value based on the whole rectangle. In order to compute the SD for this value, two other CNRs values were also computed based on 2 smaller rectangles within predefined rectangles. The SDs were computed based on these three CNR values.

IV. Results

A. Experimental phantoms

Local ACS maps obtained with both PF and SLD methods for models A - E are presented in Fig. 3 and Fig. 4. Maps without regularization are presented first, and then compared with those obtained with regularization (indicated with -R). In the bottom row of Fig. 3 and Fig. 4, mean ACS values for different axial positions are compared with ground truth (±SD) measurements obtained with the planar reflection method, which are 0.56 ± 0.07 dB cm^{-1} MHz^{-1} (for 4.5% graphite powder concentration, medium #1) and 1.15 ± 0.10 dB cm^{-1} MHz^{-1} (for 12% concentration, medium #2), respectively.

Biases and NRMSE obtained by PF and SLD methods for phantom models A - E are presented in Table I. The bias in dB cm^{-1} MHz^{-1} for the first homogeneous phantom (model A) with three acquisitions was close in absolute value for PF, PF-R, SLD, SLD-R, and RFM at -0.06 ± 0.03, 0.04 ± 0.07, -0.09 ± 0.06, -0.06 ± 0.05, and -0.15 ± 0.07, respectively. Same trends were emphasized for the second more attenuating homogeneous phantom (model B). Biases for the PF, PF-R, SLD, SLD-R, and RFM were 0.26 ± 0.12, -0.07 ± 0.02, -0.32 ± 0.11, -0.10 ± 0.05, and -0.23 ± 0.18, respectively. As indicated in Table I, trends in favor of the PF-R method were confirmed when analyzing NRMSEs. Results show that the PF-R method yielded lower NRMSEs compared with SLD-R and RFM, and those differences were emphasized without regularization for SLD. The largest mean of biases and NRMSEs were obtained with the SLD method that was used in this study for comparison.

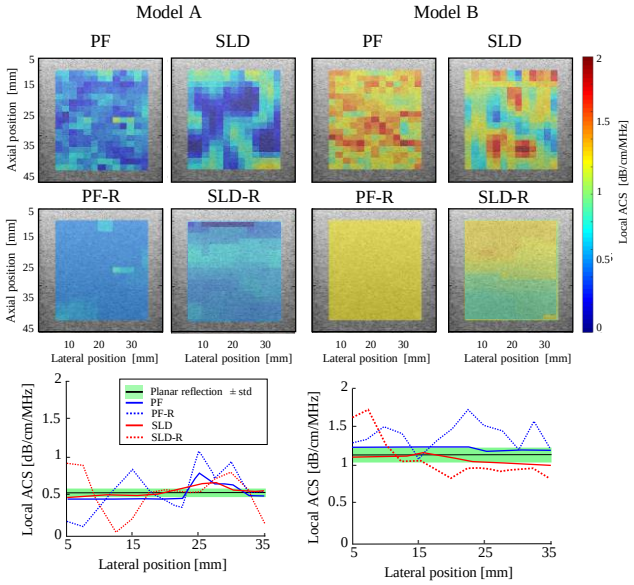

Fig. 3. Local attenuation maps obtained with phantom free (PF) and spectral log-difference (SLD) methods for experimental phantoms with medium #1 (model A) and medium #2 (model B). The first and second rows show attenuation maps without and with regularization (R), respectively. The bottom row presents the comparison of mean ACS estimated with PF, PF-R, SLD and SLD-R methods for the two models. Green regions in graphs of bottom row show means and standard deviations for ground truth measurements with the planar reflection method.

With side-by-side and top-to-bottom media (models C, D and E), each based on 3 acquisitions, biases and NRMSEs were either smaller, similar or higher than for homogeneous phantoms (Table I). Biases and NRMSEs obtained with the PF-R method were generally less for both media. The PF-R had the highest CNR compare to the other methods. Furthermore, according to the bottom row of Fig. 4, the PF with regularization made a distinct differentiation at the boundary of both media, whereas the SLD method with regularization had a smoother transition.

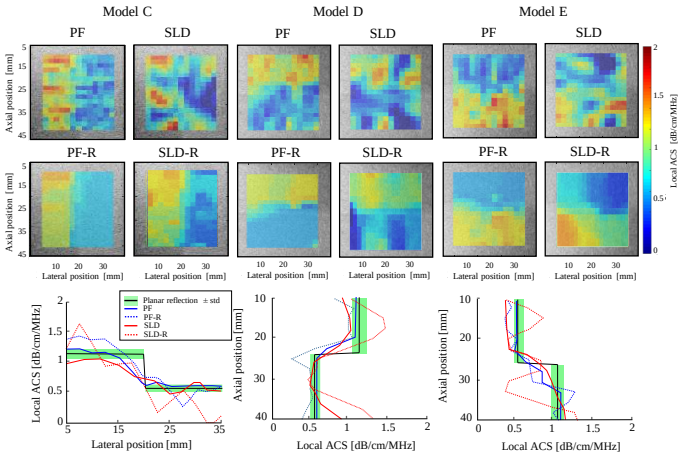

Fig. 4. Local attenuation maps obtained with phantom free (PF) and spectral log-difference (SLD) methods for experimental phantoms with side-by-side medium #1 on the right and #2 on the left (model C), top-to-bottom medium #1 on the bottom and #2 on the top (model D), and vice versa (model E). The first and second rows show attenuation maps without and with regularization (R), respectively. The bottom row presents the comparison of mean ACS estimated with PF, PF-R, SLD, and SLD-R methods for the three models. Green regions in graphs of the bottom row show means and standard deviations for ground truth measurements with the planar reflection method.

B. Phantoms with inclusions

Local ACS maps given by PF and SLD methods, without and with regularization, are presented graphically in the first and second rows of Fig. 5, respectively. Inclusions are visually emphasized with black dashed line circles on attenuation maps. The PF method has smoother maps than the SLD method, and inclusions are visually more detectable. After regularization, inclusions are identifiable with both PF-R and SLD-R methods. According to Table II, in the case of smaller inclusions of 10 and 15 mm diameters, the biases within inclusions were larger and the NRMSE were less with the PF method compare to SLD. On the other hand, the PF had a better estimation of ACS outside inclusions (lower biases and NRMSEs), *i.e.* within homogeneous regions of phantoms. For the largest inclusion of 20 mm, the bias of the PF method is higher than for the SLD method within the inclusion. However, it is the other way around in the surrounding tissue. The average of absolute bias values of both regions of phantoms with the PF and PF-R methods are generally less than with the SLD and SLD-R methods. The same trend was observed with NRMSE values. After regularization, the bias and NRMSE in all regions are decreased; PF-R with regularization had the lowest mean biases and NRMSEs over all inclusion phantoms. It shows that the regularization increased CNR values for both PF and SLD methods. Higher CNRs were obtained for bigger inclusions with the PF-R method. PF-R and SLD-R had similar CNRs in the case of the 10 mm diameter inclusion.

According to the bottom row of Fig. 5, the SLD-R method has smoother transitions between the surrounding tissue and the inclusion, thus reducing the lesion detectability but improving the size detection compared with the proposed method. Differences tend to disappear for the larger inclusion of 20 mm. In general, ACS results with the proposed regularized method (PF-R) are closer to ground truth values.

TABLE I

COMPARISON OF BIASES, NORMALIZED ROOT-MEAN-SQUARED ERRORS (NRMSE), AND CONTRAST-TO-NOISE RATIOS (CNR) FOR ATTENUATION MAPS OF PHANTOMS CORRESPONDING TO MODELS A - E OBTAINED WITH THE PROPOSED PHANTOM FREE (PF), SPECTRAL LOG-DIFFERENCE (SLD), AND REFERENCE FREQUENCY METHOD (RFM), BEFORE AND AFTER REGULARIZATION (R).

		PF		**PF-R**		**SLD**		**SLD -R**		**RFM**	
Model		Medium #1	Medium #2	Medium #1	Medium #2	Medium #1	Medium #2	Medium #1	Medium #2	Medium #1	Medium #2
A	Bias (dB/cm/MHz)	-0.06 ± 0.03	-	0.04 ± 0.07	-	-0.09 ± 0.06	-	-0.06 ± 0.05	-	-0.15 ± 0.07	-
	NRMSE (%)	15.1 ± 2.1	-	8.9 ± 3.6	-	51.2 ± 5.1	-	19.2 ± 5.1	-	62.0 ± 10.6	-
B	Bias (dB/cm/MHz)	-	0.26 ± 0.12	-	-0.07 ± 0.02	-	-0.32 ± 0.11	-	-0.10 ± 0.08	-	-0.23 ± 0.18
	NRMSE (%)	-	13.5 ± 1.0	-	7.0 ± 1.6	-	42.6 ± 8.2	-	18.85 ± 6.1	-	34.9 ± 9.6
C	Bias (dB/cm/MHz)	0.09 ± 0.07	0.10 ± 0.06	0.05 ± 0.01	-0.01 ± 0.07	-0.07 ± 0.23	0.23 ± 0.23	-0.07 ± 0.18	-0.11± 0.12	-	-
	NRMSE (%)	35.1 ± 2	44.3 ± 1.2	11.3 ± 1.0	21.2 ± 5.0	45.6 ± 4.9	49.2 ± 6.3	19.2 ± 4.3	25.3 ± 8.1	-	-
	CNR	1.74 ± 0.07		3.54 ± 0.41		0.86 ± 0.04		1.75 ± 0.09		-	-
D	Bias (dB/cm/MHz)	0.06 ± 0.08	0.07 ± 0.03	0.04 ± 0.06	0.01 ± 0.05	-0.08 ± 0.31	0.18 ± 0.11	-0.06 ± 0.13	-0.14 ± 0.11	-	-
	NRMSE (%)	30.3 ± 3.2	38.4 ± 0.2	10.1 ± 3.2	17.4 ± 0.02	41.7 ± 5.2	45.2 ± 2.1	17.2 ± 3.4	20.3 ± 5.1	-	-
	CNR	1.72 ± 0.08		2.66 ± 0.31		0.70 ± 0.09		2.09 ± 0.14		-	-
E	Bias (dB/cm/MHz)	0.05 ± 0.09	0.09 ± 0.08	0.05 ± 0.02	0.08 ± 0.05	-0.13 ± 0.12	0.11 ± 0.13	-0.11 ± 0.07	-0.08 ± 0.13	-	-
	NRMSE (%)	30.3 ± 3.2	45.4 ± 7.2	9.3 ± 2.2	22.4 ± 8.6	43.9 ± 7.2	49.2 ± 6.3	27.3 ± 5.4	24.2 ± 7.1	-	-
	CNR	1.72 ± 0.12		3.41 ± 0.6		0.79 ± 0.13		2.12 ± 0.35		-	-

Table II

COMPARISON OF BIASES, NORMALIZED ROOT-MEAN-SQUARED ERRORS (NRMSE), AND CONTRAST-TO-NOISE RATIOS (CNR) FOR ATTENUATION MAPS OF PHANTOMS WITH INCLUSION DIAMETERS OF 10 MM, 15 MM, AND 20 MM OBTAINED WITH THE PROPOSED PHANTOM FREE (PF) AND SPECTRAL LOG-DIFFERENCE (SLD) METHODS, WITHOUT AND WITH REGULARIZATION (R).

		PF		PF-R		SLD		SLD -R	
D		Inclusion	Tissue	Inclusion	Tissue	Inclusion	Tissue	Inclusion	Tissue
10 mm	Bias (dB/cm/MHz)	-0.20 ± 0.06	-0.10 ±0.04	-0.16 ± 0.07	-0.04 ± 0.05	-0.07 ± 0.18	-0.25 ± 0.12	-0.08 ± 0.21	0.11 ± 0.09
	NRMSE (%)	33.1 ± 6.7	26.2 ±5.1	22.0 ± 6.2	25.4 ± 8.1	53.1 ± 9.1	63.2 ± 5.3	42.7 ± 5.6	32.7 ± 9.4
	CNR	0.86 ± 0.24		1.26 ± 0.38		0.59 ± 0.17		0.91 ± 0.13	
15 mm	Bias (dB/cm/MHz)	-0.26 ± 0.08	-0.13 ± 0.04	-0.14 ± 0.12	-0.05 ± 0.09	-0.17 ± 0.15	0.26 ± 0.21	-0.08 ± 0.21	0.19 ± 0.17
	NRMSE (%)	31.2 ± 6.3	36.3 ± 16.1	15.1 ± 5.0	21.2 ± 7.1	47.2 ± 9.3	90.3 ± 25.2	32.18 ± 6.4	59.7 ± 15.1
	CNR	0.87 ± 0.41		1.05 ± 0.50		0.37 ± 0.24		0.92 ± 0.47	
20 mm	Bias (dB/cm/MHz)	-0.11 ± 0.03	-0.12 ± 0.01	-0.03 ± 0.1	-0.01 ± 0.07	-0.07 ± 0.23	0.23 ± 0.23	-0.09 ± 0.14	0.12 ± 0.14
	NRMSE (%)	25.2 ± 2.2	24.1 ± 1.1	11.7 ± 0.03	16.2 ± 1	40.3 ± 8.2	106.0 ± 29.2	13.1 ± 7.5	82.5 ± 41.7
	CNR	1.40 ± 0.46		1.63 ± 0.63		0.38 ± 0.23		1.37 ± 0.24	

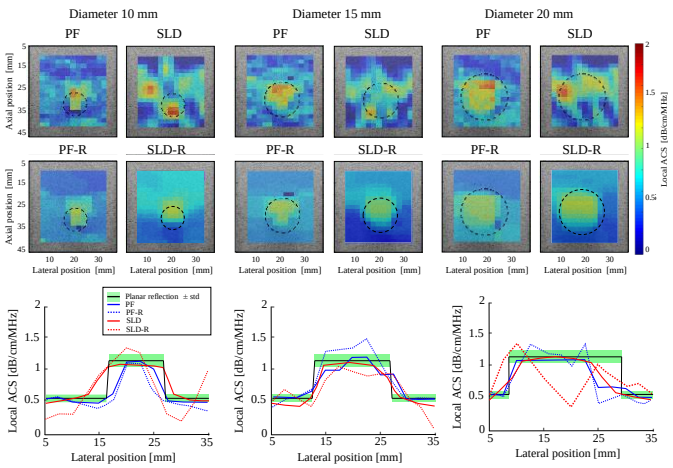

Fig. 5. Local attenuation maps for experimental phantoms with inclusion diameters of 10 mm, 15 mm, and 20 mm with phantom free (PF) and spectral log-difference (SLD) methods. The first and second rows show attenuation maps without and with regularization (R), respectively. The bottom row presents the comparison of mean ACS estimated with PF, PF-R, SLD, and SLD-R methods for the three inclusion sizes. Green regions in graphs of bottom row show means and standard deviations for ground truth measurements with the planar reflection method.

Overall, the mean of absolute biases from the 55 experimental datasets including homogeneous, side-by-side, top-to-bottom, and inclusion phantoms were 0.17 ± 0.06, 0.14 ± 0.05, 0.23 ± 0.07 and 0.20 ± 0.07 dB cm^{-1} MHz^{-1} ($p < 0.001$) for PF, PF-R, SLD, and SLD-R methods, respectively. Mean NRMSEs of PF, PF-R, SLD, and SLD-R methods from all 55 datasets were 41.7 ± 10.2, 32.9 ± 12.9, 76.0 ± 27.5 and 46.1 ± 19.4 % (p <0.001), respectively. Also, mean of CNRs from 45 experimental datasets including side-by-side, top-to-bottom, and inclusion phantoms were 1.18 ± 0.49, 1.69 ± 0.95, 0.51 ± 0.21 and 1.37 ± 0.62 (p <0.001) with PF, PF-R, SLD, and SLD-R methods, respectively. This comparison shows that the PF method with regularization had the lowest biases and NRMSEs, and highest CNRs.

The PF and PF-R methods were also investigated with a median filter; the biases and NRMSEs are provided in Table III. Results with median filtering of ACS maps are given in Fig. 6.

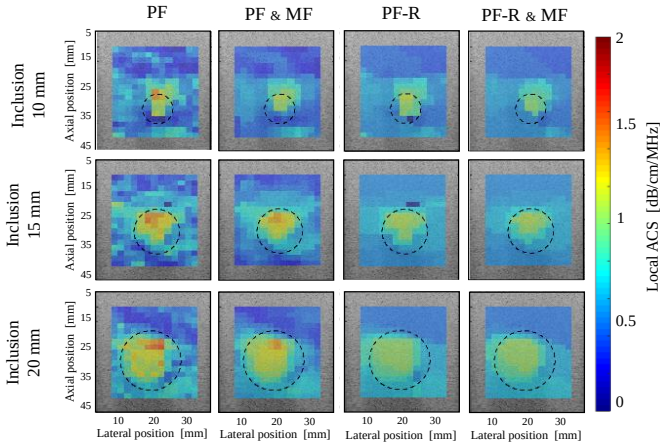

Fig. 6. Local attenuation maps for experimental phantoms with inclusions of 10 mm, 15 mm, and 20 mm using the phantom free (PF), the same method after applying a median filter (PF & MF), the PF method with regularization (PF-R), and results with PF-R and median filtering (PF-R & MF)

Table III

COMPARISON OF BIASES, NORMALIZED ROOT-MEAN-SQUARED ERRORS (NRMSE), AND CONTRAST-TO-NOISE RATIOS (CNR) FOR ATTENUATION MAPS OF PHANTOMS WITH INCLUSION DIAMETERS OF 10 MM, 15 MM, AND 20 MM OBTAINED AFTER APPLYING A MEDIAN FILTER ON RESULTS OF THE PHANTOM FREE METHOD (PF) OR PHANTOM FREE METHOD WITH REGULARIZATION (PF-R).

		PF with median filter		PF–R with median filter	
D		Inclusion	Tissue	Inclusion	Tissue
10 mm	Bias (dB/cm/MHz)	-0.30 ± 0.05	-0.06 ± 0.04	-0.21 ± 0.06	-0.08 ± 0.05
	NRMSE (%)	29.0 ± 6.5	25.7 ± 4.2	22.0 ± 2.1	25.4 ± 6.1
	CNR	0.87 ± 0.21		1.29 ± 0.35	
15 mm	Bias (dB/cm/MHz)	-0.23 ± 0.08	-0.10 ± 0.05	-0.15 ± 0.06	-0.06 ± 0.06
	NRMSE (%)	23.2 ± 7.5	34.2 ± 7.3	14.1 ± 5.02	21.2 ± 0.04
	CNR	0.92 ± 0.45		1.15 ± 0.47	
20 mm	Bias (dB/cm/MHz)	-0.06 ± 0.2	-0.09 ± 0.09	-0.04 ± 0.07	-0.01 ± 0.04
	NRMSE (%)	17.0 ± 2.2	21.7 ± 1.1	10.2 ± 3.4	14.2 ± 6.01
	CNR	1.44 ± 0.44		1.69 ± 0.59	

According to Table III, the NRMSE for the PF method with median filtering in both regions of phantoms are smaller in comparison with the PF method (based on Table II), and absolute values of biases are also smaller, except in the case of the smallest inclusion (diameter of 10 mm). Moreover, the PF with regularization has smaller biases and NRMSEs, and also larger CNRs, compared with the median filtered PF method. With median filtering on PF-R results, absolute values of biases and CNRs are larger compared with the proposed PF-R method, but NRMSEs are smaller.

C. In-vivo human livers

In this section, as for phantom experiments, results of PF and SLD methods are compared based on mean values and CVs within tumors and surrounding tissues. Also, CNRs are compared for attenuation maps obtained in the case of liver cancers.

1. Nonalcoholic steatohepatitis

The left columns of Fig. 7(a) and Fig. 7(b) display the B-mode image and the ROI under investigation (red box) for livers with MRI fat fractions of 0.61% and 15.01%, respectively. For the healthy liver, means ± standard deviations in dB cm^{-1} MHz^{-1} obtained for PF and SLD methods are 0.45 ± 0.28 and 0.51 ± 0.47 without regularization, and 0.47 ± 0.20 and 0.67 ± 0.11 with PF-R and SLD-R, respectively. The smallest variability was obtained with the SLD-R method (CV of 16.4%). Similarly, local attenuation maps of the steatotic grade 2 liver provided ACS values for PF and SLD methods of 0.92 ± 0.19 and 1.14 ± 0.41 dB cm^{-1} MHz^{-1}, and after regularization these values are 0.91 ± 0.08 and 1.06 ± 0.15 for PF-R and SLD-R, respectively. The PF-R method resulted in the smallest CV (8.8%) but differences in mean values are small.

2. Liver cancers

Local attenuation maps without regularization estimated by PF and SLD methods for the human liver with a HCC cancer are shown in the top row of Fig. 8(a). The detection and diagnosis of the lesion based on MRI was visually registered on US images. Yellow boxes on B-mode images show the position of the ROI within the liver, which includes the lesion.

For CNR computations in Fig. 8, the position of the lesion and liver parenchyma on attenuation maps are displayed with black and white dashed-line rectangles, respectively. Means ± standard deviations in dB cm^{-1} MHz^{-1}, and CNRs obtained for PF, PF-R, SLD and SLD-R methods are provided in Table IV.

The lesion could be deduced from the ACS map produced by the PF method (localized spot with high attenuation) but in the case of the SLD method, several scattered areas with varying attenuations could be suspected as being a lesion. After regularization (bottom row of Fig. 8(a)), the lesion is visible on the PF map as a homogeneous area with the highest attenuation but detectability on the regularized SLD map is less apparent. This could be also deduced from computed CNRs.

Both PF-R and SLD-R methods underestimated the size of the tumor compared with the B-mode counterpart. Maximum ACS values within the ROI containing the HCC lesion are 1.41 and 1.37 dB cm^{-1} MHz^{-1} for PF-R and SLD-R methods, respectively. The position of the maximum attenuation coefficient within the map did not coincide between methods.

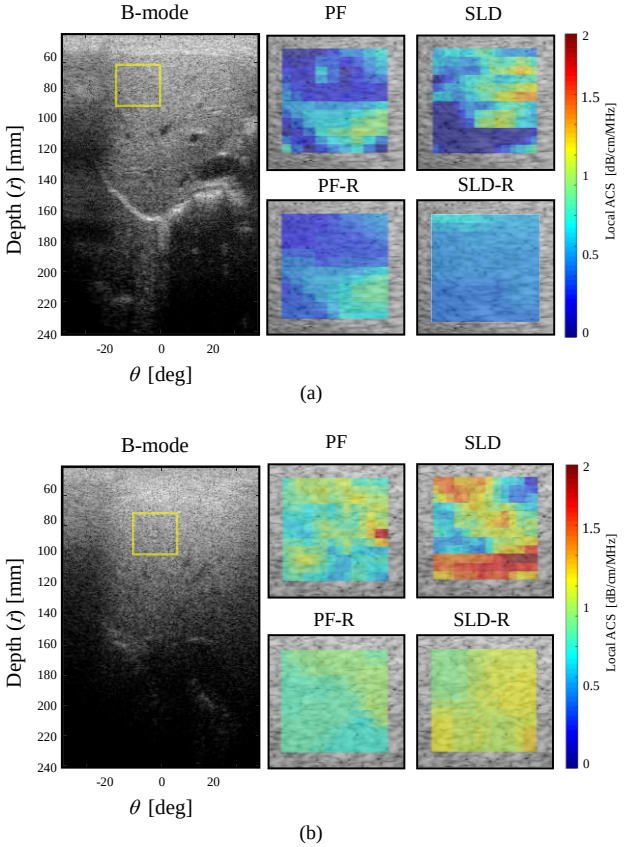

Fig. 7. ACS results for two *in-vivo* human NAFLD datasets with MRI-determined proton density fat fractions of 0.6% (corresponding to a histological grade S0) (A, woman of 25 years old) and 15.0% (corresponding to a histological grade S2) (B, woman of 52 years old), respectively. For each participant, the B-mode image and the ROI (red box) under investigation are presented, along with local attenuation maps within the ROI for phantom free (PF) and spectral log-difference (SLD) methods (without and with regularization in the first and second rows, respectively).

Fig. 8(b) shows the second *in-vivo* human liver dataset corresponding to a metastatic liver cancer. Maps produced by the PF method whether regularization was used or not allow to clearly detect a lesion with high attenuation in the middle of the ROI, whereas detectability is more difficult on SLD maps. Maximum ACS values within the ROI with PF-R and SLD-R methods are 1.74 and 1.29 dB cm^{-1} MHz^{-1}, respectively. The PF-R method had the highest CNR compared to other methods.

V. Discussion

In this work, we demonstrated the theoretical basis for estimating local ACS without the need of a calibration phantom

TABLE IV

COMPARISON OF MEANS AND CONTRAST-TO-NOISE RATIOS (CNR) FOR ATTENUATION MAPS OF TWO *IN-VIVO* HUMAN LIVER DATASETS WITH CANCER. (A) LIVER HEPATOCELLULAR CARCINOMA IN THE RIGHT LOBE OF A 55-YEAR-OLD MAN; (B) COLORECTAL LIVER METASTASIS IN THE LEFT LOBE OF A 67-YEAR-OLD WOMAN. MEANS AND CNRS ARE COMPUTED BASED ON RECTANGLE AREAS WITHIN THE LESION AND PARENCHYMA TISSUES.

		PF		PF-R		SLD		SLD -R	
Liver Cancer		Lesion	Tissue	Lesion	Tissue	Lesion	Tissue	Lesion	Tissue
(a)	Mean (dB/cm/MHz)	0.95 ± 0.33	0.59 ± 0.19	1.01 ± 0.21	0.57 ± 0.10	1.12 ± 0.34	0.48 ± 0.39	1.08 ± 0.17	1.13± 0.24
	CNR	1.73 ± 0.76		2.31 ± 0.37		1.72 ± 0.58		2.02 ± 0.31	
(b)	Mean (dB/cm/MHz)	1.53 ± 0.23	0.67 ± 0.42	1.40 ± 0.26	0.56 ± 0.19	0.84 ± 0.48	0.47 ± 0.34	0.91 ± 0.22	0.72 ± 0.13
	CNR	2.34 ± 0.92		3.41 ± 1.14		0.95 ± 0.43		1.73 ± 0.82	

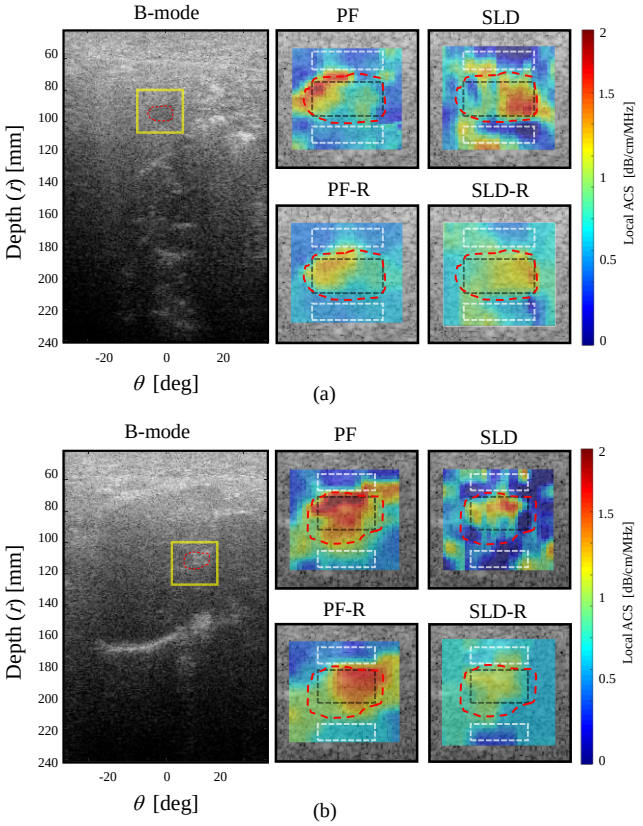

Fig. 8. Results for two *in-vivo* human liver datasets with cancer: (a) liver hepatocellular carcinoma in the right lobe of a 55-year-old man; (b) colorectal liver metastasis in the left lobe of a 67-year-old woman. For each participant, the B-mode image is presented on the left with the identified ROI (red box) including the lesion. On the right is shown local attenuation maps with phantom free (PF) and spectral log-difference (SLD) methods without (top row) and with regularization (bottom row). The lesion positions are indicated with red dashed-lines. The lesion and parenchyma tissue regions used for computing CNRs are indicated with black and white dashed-line rectangles, respectively.

in the context of heterogeneous media, thus extending the work of Gong *et al.* [42], which was considering homogeneous structures. We also integrated the proposed PF method into a theoretical framework yielding regularized local ACS maps.

A method such as the SLD can be quite cumbersome for clinical trials because a phantom acquisition is necessary after the clinical US exam using the same probe and system settings. As mentioned, the proposed method was inspired from the RFM of Gong *et al.* [42], with the following novelties: a linear interpolation of the power spectrum in log-scale was used, the underlying hypothesis on the compression wave US probe diffraction factor was relaxed, a generalization to heterogeneous local ACS was made, and an adaptive restriction on usable frequencies was implemented to consider a more reliable range than the usual -20 dB frequency range. Moreover, the framework of the regularization scheme proposed in our preliminary reports [31, 43] was better documented and also implemented in the framework of the SLD method. We could demonstrate equivalent or even smaller biases and NRMSEs than the classical SLD method on the *in-vitro* dataset, and equivalent or larger CNRs on the *in-vivo* liver data. The addition of regularization to both proposed PF and classical SLD methods further allowed appreciating the performance of the phantom-free algorithm. Furthermore, applying a median filter could also further reduce image variability, but it showed limitation in the case of small inclusion phantoms as filtering blurred boundaries. The overall procedure for constructing local ACS maps in this work is schematized in Fig. 9.

ACS estimates on both homogeneous and heterogeneous tissues represented a specific challenge, rarely addressed in the scientific literature [30]. The implementation of strategies listed in Fig. 2 allowed obtaining promising phantom and proof-of-concept clinical results. Results based on the PF-R method on homogeneous, side-by-side, and top-to-bottom phantoms indicated that the proposed method could estimate ACS close to ground truth values, and in all cases, NRMSEs decreased with regularization, which allowed differentiating visually the two media. CNRs also increased with regularization. The comparison of PF with the SLD algorithm showed that the proposed method had a better prediction at the border between two media. Producing phantoms with top-to-bottom designs was of particular interest as it could mimic the more attenuating superficial thick layer of fat in patients with obesity (model D), or the accumulation of low-attenuating fluid in the liver of patients with ascites (model E).

The performance of the proposed method for detecting lesions in experimental phantoms with diameters varying from 10 to 20 mm was also investigated. Results showed that the

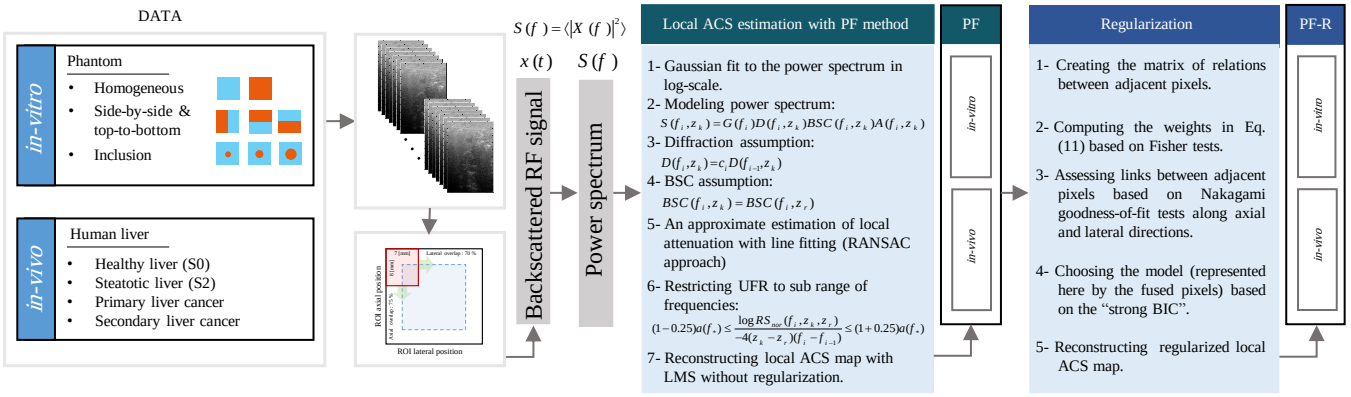

Fig. 9. Summary of the proposed procedure for constructing local ACS maps with PF and PF-R methods on *in-vitro* and *in-vivo* data.

proposed method could detect all lesions. Regularization increased the CNRs by reducing variances in both the inclusion and its surrounding. Since the CNR depends on mean values and variances within the inclusion and surrounding tissues, we do not expect a trend of CNR with the inclusion's size. This can be observed in the values reported in Table II.

We also examined the influence of a median filter on attenuation maps of the PF method without and with regularization. The regularization had lower biases and NRMSEs compared with a simple median filtering. Applying filters on regularized attenuation maps could further improve results due to the smoothening effect on ACS maps and increase in CNRs, which is a common task in image processing [56]. Notice that in the case of small inclusions, a median filter can increase the bias and blur boundaries, which are not desirable.

The proposed method was also tested on two *in-vivo* human NAFLD data. Results obtained were in the range of values reported in the literature [57-59]. The proposed method provided smaller variability than SLD for each clinical case. Coefficients of variation showed reduction after regularization. Differences between both datasets in terms of local ACS were observed, and the liver with a steatosis grade 2 showed a higher attenuation. This is in line with recent clinical reports using clinical systems where ACS could correlate with the MRI-PDFF or biopsy staging. According to recent works, attenuation had increasing trends with higher steatosis grades [60, 61]. Therefore, this method may be utilized as a biomarker for diagnosis of liver steatosis.

Finally, the proposed method was evaluated in the case of two *in-vivo* human livers with cancer. Lesions were detectable with both PF and SLD methods with regularization. The higher attenuation coefficient on liver images of patients with secondary cancer than primary HCC (as seen in Fig. 8) was also recently observed in therapeutic US applications; in this report, however, no attenuation images were provided [62].

To our knowledge, ACS imaging has not yet been used for detecting and characterizing liver cancer. In addition to the fact that the proposed method does not use a reference phantom for ACS estimation, our proof-of-concept on liver cancer datasets is opening the opportunity to use this new imaging contrast for the diagnosis of liver cancer.

One of the limitations of this work is that only one computation window size was consider to reconstruct attenuation maps for both PF and SLD methods. There is always a trade-off between resolution and accuracy of estimation. Hence, additional studies are needed to find the optimum CW's size for a specific clinical application without affecting too much the resolution of attenuation maps. There are also other types of regularization that may improve the reconstruction of parametric maps [34, 35]. Moreover, the size of CWs could affect the Nakagami model, especially in the case of long CWs. Also, overlapping of CWs could prevent the assumption of independent identically distributed residual noise to hold, although it is common to make this assumption in the case of overlapping windows [34, 63]; this potential issue should be investigated in future studies. Furthermore, although the power spectrum of backscattered RF signals is assumed approximately Gaussian in many medical ultrasound applications [64], there are nonetheless cases where this assumption would not hold. However, other models could be adopted to fit power spectra [65], an avenue which could be investigated in future studies.

Finally, based on obtained *in-vivo* results, the proposed method may certainly provide additional information to clinicians for the diagnosis of liver steatosis and detection of suspected cancerous lesions visible on B-mode US. The ultimate goal would be to improve the detection of HCC in early stages when it is not visible on B-mode images.

VI. Conclusion

A method, inspired by the work of Gong *et al*. [42], was presented for estimating local ACS based on frequency and depth normalization without the need of a calibration phantom. The proposed method was tested on homogeneous, side-by-side, top-to-bottom, and heterogeneous phantoms with inclusions. Also, the performance of the proposed method was assessed in the case of four *in-vivo* human livers consisting of one normal case, one stage 2 steatotic liver, one liver with a primary hepatocellular carcinoma and one with a secondary metastatic cancer. The proposed method uses linear interpolation of the power spectrum in log-scale, the relaxation of the underlying hypothesis on the wave diffraction factor, and an adaptive restriction of frequencies to a more reliable range than the usual -20 dB usable frequency range. Moreover, a generalization to nonhomogeneous local ACS has been proposed. Furthermore, a regularization procedure, which was

formulated as a generalized LASSO, and a variant of the Bayesian Information Criterion were applied to estimate the Lagrangian multiplier on the LASSO constraint. It was shown that applying regularization overall improved local ACS maps. In future works, further validation on larger *in-vivo* datasets should be conducted, and the performance of the proposed method with different beamforming approaches should also be investigated.

APPENDIX A

The data fidelity term and constraint matrix of Section II.C are explained in the case of the SLD model in this appendix. Let us recall that in the SLD method, one considers two non-overlapping windows within the CW at proximal and distal depths z_p and z_d, respectively. Attenuation factors at depths z_p and z_d, for either samples or the reference phantom, are of the form:

$$A(f, z_p) = \exp(-4\alpha_{total} z_p f); \quad \text{(A-1a)}$$

$$A(f, z_d) = \exp(-4(\alpha_{total} z_p + \alpha_{local}\Delta z) f), \quad \text{(A-1b)}$$

where α_{total} and α_{local} denote the total and local ACS, respectively, and $\Delta z = z_d - z_p$. Furthermore, one assumes that backscatter coefficients at two depths within an ROI are proportional, which under the Gaussian scattering model means that the effective scatterers' radius remains fixed within the ROI, but that the acoustic concentration might vary [15]. One then computes the relation [15]:

$$\log\frac{PS_S(f, z_p)}{PS_S(f, z_d)} - \log\frac{PS_{ref}(f, z_p)}{PS_{ref}(f, z_d)} = 4\Delta\alpha_{local}\Delta z f + const, \quad \text{(A-2)}$$

where $\Delta\alpha_{local}$ is the difference in local ACS between samples and the reference phantom. Thus, the observed spectral data in the left-hand side of (A-2) are:

$$y_r = \left(\log\frac{PS_S(f, z_p)}{PS_S(f, z_d)} - \log\frac{PS_{ref}(f, z_p)}{PS_{ref}(f, z_d)}\right)_{i=1}^{N_{Freq}}. \quad \text{(A-3a)}$$

The predictors' matrix and regression coefficients are finally of the form:

$$X_r = (4f_i\Delta z_r \quad 1)_{i=1}^{N_{Freq}}; \quad \text{(A-3b)}$$

$$\beta_r = (\beta_{r,1} \quad \beta_{r,2})^T; \quad \text{(A-3c)}$$

$$\beta_{r,1} = \Delta\alpha_{r,local}. \quad \text{(A-3d)}$$

The weights w_r in Eq. (11) were kept to 1.

Since, in the case of the SLD model, the vector of regression coefficients has dimension d greater than 1 ($d = 2$), its components might be of different order of magnitude. Thus, the ℓ_1-norm regularization term in Eq. (13a) was replaced with

$$reg_1(\beta, \lambda) = \lambda\sum_{r=1}^{N_{CW}}\sum_{m=1}^{d} a_m \sum_{s\in N(r)} |\beta_{r,m} - \beta_{s,m}|, \quad \text{(A-4a)}$$

where a_m, $m = 1, 2$, are the weights of the regression coefficients. The LMSE problem was first solved without regularization, and then the weights were set to

$$a_1 = \frac{\dfrac{1}{\left\|(\beta_{r,1} + \alpha_{ref})\right\|_1}}{\dfrac{1}{\left\|(\beta_{r,1} + \alpha_{ref})\right\|_1} + \dfrac{1}{\left\|(\beta_{r,2})\right\|_1}}; \quad \text{(A-4b)}$$

$$a_2 = \frac{\dfrac{1}{\left\|(\beta_{r,2})\right\|_1}}{\dfrac{1}{\left\|(\beta_{r,1} + \alpha_{ref})\right\|_1} + \dfrac{1}{\left\|(\beta_{r,2})\right\|_1}}, \quad \text{(A-4c)}$$

where $(\beta_{r,1}, \beta_{r,2})$ denotes the initial LMSE solution. In particular, sum up to 1, the terms in Eq. (A-4a) are now of comparable order of magnitude.

APPENDIX B

In this section, the comparison between RFM and the proposed method is provided by considering each modification brought to the RFM (see the impact of each step implementation in Table B-I). As mentioned in [42, 66], the RFM has been used only in the case of a homogeneous medium, and a square computation window of about 2.5 cm side length was considered.

The most important innovations in our work can be summarized into the following features: A) the smaller CW's size; B) the usable frequency range (UFR); C) the log-scale Gaussian fit; D) the adaptive frequency sub-range of the UFR, and E) the modified RANSAC line fitting.

In the initial state of the method (Gong *et al*., 2019, [42]), the CW was a square with sides of 2.5 cm and the frequency range was fixed between 4 to 6 MHz. With this configuration in Table B-I, the RFM had a good estimation of attenuation on the first

TABLE B-I
COMPARISON OF RFM AND PF METHODS ON TWO HOMOGENEOUS PHANTOMS AND INVESTIGATION OF THE EFFECT OF EACH MODIFICATION

	Method	Modifications					Bias Medium #1 (dB cm^{-1} MHz^{-1})	R	Bias Medium #2 (dB cm^{-1} MHz^{-1})	R
		A	B	C	D	E				
1	RFM	2.5 cm	4-6 MHz				-0.15		-0.23	
2		✓	4-6 MHz				0.97	0.81	-0.40	-0.33
3		✓	✓				0.38		-0.20	
4		✓	✓	✓			-0.37		-0.54	
5		✓	✓	✓	✓		0.12		0.48	
6	Proposed	✓	✓	✓	✓	✓	0.06	0.04	0.26	-0.07

A: Computing window (size = 0.7 cm), B: usable frequency range (UFR), C: log-scale Gaussian fit, D: adaptive frequency sub-range, E: modified RANSAC approach, and R: regularization

phantom (bias of -0.15) but a larger underestimation on the second phantom (bias of -0.23).

In the second state (condition A), the CW size was decreased (as in our implementation of PF and SLD methods). It can be observed that the RFM failed with such a small window's size and even the estimated attenuation for medium #2 was less than for medium #1, which should be the opposite trend. In the third state (condition A+B), by changing the frequency range used in RFM (4-6 MHz) to the UFR, the biases for both phantoms decreased, and the attenuation estimated for medium #2 was slightly higher than medium #1, but the biases were still large. In the fourth state (conditions A+B+C), a log scale Gaussian fit was applied to the previous improvements. It can be observed that although the bias for medium #2 was increased, the difference in estimated attenuation for the two media was nevertheless larger. In the fifth state (conditions A+B+C+D), by considering the adaptive frequency range within the URF, the biases were much smaller in both cases and the trend of estimated attenuations was correct in both media. For the final improvement considered with the proposed method (the sixth state, conditions A+B+C+D+E), by adding the proposed modified RANSAC line fitting criterion, the biases were much reduced.

We also considered comparing the RFM and the proposed method with regularization. However, it was not applicable with the large CW size recommended by Gong *et al*. [42, 66] due to a resulting lack of memory, as this implies several sub-windows. Nonetheless, regularization was performed on the RFM with small CWs (state 2). The resulting absolute biases were larger than those obtained with the proposed method either with or without regularization.

ACKNOWLEDGMENT

Authors acknowledge the contribution of Marie-Hélène Roy Cardinal (B. Eng., Ph.D.) and Boris Chayer (B. Eng., M. Eng.) for helpful discussions and suggestions on statistics and phantom fabrication, respectively.

REFERENCES

[1] H. B. El-Serag, and K. L. Rudolph, "Hepatocellular carcinoma: epidemiology and molecular carcinogenesis," *Gastroenterology,* vol. 132, no. 7, pp. 2557-2576, Jun, 2007.

[2] J. M. Llovet, R. K. Kelley, A. Villanueva *et al.*, "Hepatocellular carcinoma," *Nature Reviews Disease Primers,* vol. 7, no. 1, pp. 6 (28 pages), Jan, 2021.

[3] A. Villanueva, "Hepatocellular carcinoma," *New england journal of medicine,* vol. 380, no. 15, pp. 1450-1462, Apr, 2019.

[4] J. D. Yang, P. Hainaut, G. J. Gores *et al.*, "A global view of hepatocellular carcinoma: trends, risk, prevention and management," *Nature Reviews Gastroenterology & Hepatology,* vol. 16, no. 10, pp. 589-604, Oct, 2019.

[5] W. Wang, and C. Wei, "Advances in the early diagnosis of hepatocellular carcinoma," *Genes & Diseases,* vol. 7, no. 3, pp. 308-319, Sep, 2020.

[6] S. M. Bierig, and A. Jones, "Accuracy and cost comparison of ultrasound versus alternative imaging modalities, including CT, MR, PET, and angiography," *Journal of Diagnostic Medical Sonography,* vol. 25, no. 3, pp. 138-144, May, 2009.

[7] A. Singal, M. L. Volk, A. Waljee *et al.*, "Meta-analysis: surveillance with ultrasound for early-stage hepatocellular carcinoma in patients with cirrhosis," *Aliment Pharmacol Ther,* vol. 30, no. 1, pp. 37-47, Jul, 2009.

[8] A. Colli, M. Fraquelli, G. Casazza *et al.*, "Accuracy of ultrasonography, spiral CT, magnetic resonance, and alpha-fetoprotein in diagnosing hepatocellular carcinoma: a systematic review," *The American Journal of Gastroenterology,* vol. 101, no. 3, pp. 513-523, Mar, 2006.

[9] R. Chou, C. Cuevas, R. Fu *et al.*, "Imaging techniques for the diagnosis of hepatocellular carcinoma: a systematic review and meta-analysis," *Annals of Internal Medicine,* vol. 162, no. 10, pp. 697-711, May, 2015.

[10] P. Del Poggio, S. Olmi, F. Ciccarese *et al.*, "Factors that affect efficacy of ultrasound surveillance for early stage hepatocellular carcinoma in patients with cirrhosis," *Clinical Gastroenterology and Hepatology,* vol. 12, no. 11, pp. 1927-33.e2, Nov, 2014.

[11] R. N. Uppot, D. V. Sahani, P. F. Hahn *et al.*, "Effect of obesity on image quality: fifteen-year longitudinal study for evaluation of dictated radiology reports," *Radiology,* vol. 240, no. 2, pp. 435-439, Aug, 2006.

[12] G. Cloutier, F. Destrempes, F. Yu *et al.*, "Quantitative ultrasound imaging of soft biological tissues: a primer for radiologists and medical physicists," *Insights into Imaging,* vol. 12, no. 1, pp. 127 (20 pages), Sep, 2021.

[13] E. A. Omari, T. Varghese, E. L. Madsen *et al.*, "Evaluation of the impact of backscatter intensity variations on ultrasound attenuation estimation," *Medical Physics,* vol. 40, no. 8, pp. 082904 (10 pages), Jul, 2013.

[14] E. Omari, H. Lee, and T. Varghese, "Theoretical and phantom based investigation of the impact of sound speed and backscatter variations on attenuation slope estimation," *Ultrasonics,* vol. 51, no. 6, pp. 758-767, Mar, 2011.

[15] Y. Labyed, and T. A. Bigelow, "A theoretical comparison of attenuation measurement techniques from backscattered ultrasound echoes," *J Acoust Soc Am,* vol. 129, no. 4, pp. 2316-2324, Apr, 2011.

[16] K. J. Taylor, C. A. Riely, L. Hammers *et al.*, "Quantitative US attenuation in normal liver and in patients with diffuse liver disease: importance of fat," *Radiology,* vol. 160, no. 1, pp. 65-71, Jul, 1986.

[17] M. Sasso, M. Beaugrand, V. de Ledinghen *et al.*, "Controlled attenuation parameter (CAP): a novel VCTE™ guided ultrasonic attenuation measurement for the evaluation of hepatic steatosis: preliminary study and validation in a cohort of patients with chronic liver disease from various causes," *Ultrasound in Medicine & Biology,* vol. 36, no. 11, pp. 1825-1835, Nov, 2010.

[18] Y. N. Zhang, K. J. Fowler, G. Hamilton *et al.*, "Liver fat imaging-a clinical overview of ultrasound, CT, and MR imaging," *The British Journal of Radiology,* vol. 91, no. 1089, pp. 20170959 (12 pages), Sep, 2018.

[19] E. Roldan-Valadez, R. Favila, M. Martínez-López *et al.*, "Imaging techniques for assessing hepatic fat content in nonalcoholic fatty liver disease," *Annals of Hepatology,* vol. 7, no. 3, pp. 212-220, Jul, 2008.

[20] C. D. Byrne, and G. Targher, "NAFLD: A multisystem disease," *Journal of Hepatology,* vol. 62, no. 1, Supplement, pp. 47-64, Apr, 2015.

[21] S. K. Venkatesh, V. Chandan, and L. R. Roberts, "Liver masses: a clinical, radiologic, and pathologic perspective," *Clinical Gastroenterology and Hepatology,* vol. 12, no. 9, pp. 1414-1429, Sep, 2014.

[22] P. H. Lima, B. Fan, J. Bérubé *et al.*, "Cost-utility analysis of imaging for surveillance and diagnosis of hepatocellular carcinoma," *American Journal of Roentgenology,* vol. 213, no. 1, pp. 17-25, Jun, 2019.

[23] T. A. Bigelow, and Y. Labyed, "Attenuation compensation and estimation," *Quantitative Ultrasound in Soft Tissues,* J. Mamou and M. L. Oelze, eds., pp. 71-93, Dordrecht: Springer Netherlands, 2013.

[24] K. J. Parker, "Ultrasonic attenuation and absorption in liver tissue," *Ultrasound in Medicine and Biology,* vol. 9, no. 4, pp. 363-369, Aug, 1983.

[25] A. M. Pirmoazen, A. Khurana, A. El Kaffas *et al.*, "Quantitative ultrasound approaches for diagnosis and monitoring hepatic steatosis in nonalcoholic fatty liver disease," *Theranostics,* vol. 10, no. 9, pp. 4277-4289, Mar, 2020.

[26] L. Castera, V. Vilgrain, and P. Angulo, "Noninvasive evaluation of NAFLD," *Nature Reviews Gastroenterology & Hepatology,* vol. 10, no. 11, pp. 666-675, Nov, 2013.

[27] O. W. Hamer, D. A. Aguirre, G. Casola *et al.*, "Fatty liver: imaging patterns and pitfalls," *RadioGraphics,* vol. 26, no. 6, pp. 1637-1653, 2006.

[28] F. M. Hooi, O. Kripfgans, and P. L. Carson, "Acoustic attenuation imaging of tissue bulk properties with a priori information," *J Acoust Soc Am,* vol. 140, no. 3, pp. 2113-2113, Sep, 2016.

[29] A. D. Pawlicki, and W. D. O'Brien, Jr., "Method for estimating total attenuation from a spatial map of attenuation slope for quantitative ultrasound imaging," *Ultrasonic Imaging,* vol. 35, no. 2, pp. 162-172, Apr, 2013.

[30] D. M. Brandner, X. Cai, J. Foiret *et al.*, "Estimation of tissue attenuation from ultrasonic B-mode images—Spectral-Log-Difference and Method-of-Moments algorithms compared," *Sensors,* vol. 21, no. 7, pp. 2548 (19 pages), Apr, 2021.

[31] F. Destrempes, M. Gesnik, and G. Cloutier, "Construction of adaptively regularized parametric maps for quantitative ultrasound imaging," in 2019 IEEE International Ultrasonics Symposium, 2019, pp. 2027-2030.
[32] H. Kim, and T. Varghese, "Hybrid spectral domain method for attenuation slope estimation," *Ultrasound in Medicine & Biology*, vol. 34, no. 11, pp. 1808-1819, Nov, 2008.
[33] M. L. Oelze, and J. Mamou, "Review of quantitative ultrasound: envelope statistics and backscatter coefficient imaging and contributions to diagnostic ultrasound," *IEEE Transactions on Ultrasonics, Ferroelectrics, and Frequency Control*, vol. 63, no. 2, pp. 336-351, Feb, 2016.
[34] A. L. Coila, and R. Lavarello, "Regularized spectral log difference technique for ultrasonic attenuation imaging," *IEEE Transactions on Ultrasonics, Ferroelectrics, and Frequency Control*, vol. 65, no. 3, pp. 378-389, Mar, 2018.
[35] F. Deeba, C. Schneider, S. Mohammed *et al.*, "SWTV-ACE: Spatially weighted regularization based attenuation coefficient estimation method for hepatic steatosis detection," in Medical Image Computing and Computer Assisted Intervention – MICCAI 2019, Cham, 2019, pp. 610-618.
[36] R. Kuc, and M. Schwartz, "Estimating the acoustic attenuation coefficient slope for liver from reflected ultrasound signals," *IEEE Transactions on Sonics and Ultrasonics*, vol. 26, no. 5, pp. 353-361, Sep, 1979.
[37] J. Ophir, T. H. Shawker, N. F. Maklad *et al.*, "Attenuation estimation in reflection: progress and prospects," *Ultrasonic Imaging*, vol. 6, no. 4, pp. 349-95, Oct, 1984.
[38] M. Insana, J. Zagzebski, and E. Madsen, "Improvements in the spectral difference method for measuring ultrasonic attenuation," *Ultrasonic Imaging*, vol. 5, no. 4, pp. 331-345, Dec, 1983.
[39] K. J. Parker, and R. C. Waag, "Measurement of ultrasonic attenuation within regions selected from B-scan images," *IEEE Transactions on Biomedical Engineering*, vol. 30, no. 8, pp. 431-437, Aug, 1983.
[40] K. Samimi, and T. Varghese, "Performance evaluation of the spectral centroid downshift method for attenuation estimation," *IEEE Transactions on Ultrasonics, Ferroelectrics, and Frequency Control*, vol. 62, no. 5, pp. 871-880, May, 2015.
[41] K. Nam, I. M. Rosado-Mendez, N. C. Rubert *et al.*, "Ultrasound attenuation measurements using a reference phantom with sound speed mismatch," *Ultrasonic Imaging*, vol. 33, no. 4, pp. 251-263, Oct, 2011.
[42] P. Gong, P. Song, C. Huang *et al.*, "System-independent ultrasound attenuation coefficient estimation using spectra normalization," *IEEE Transactions on Ultrasonics, Ferroelectrics, and Frequency Control*, vol. 66, no. 5, pp. 867-875, May, 2019.
[43] I. Rafati, F. Destrempes, and G. Cloutier, "Regularized phantom-free construction of local attenuation coefficient slope maps for quantitative ultrasound imaging," in 2020 IEEE International Ultrasonics Symposium, 2020, pp. 1-3.
[44] I. M. Rosado-Mendez, K. Nam, T. J. Hall *et al.*, "Task-oriented comparison of power spectral density estimation methods for quantifying acoustic attenuation in diagnostic ultrasound using a reference phantom method," *Ultrason Imaging*, vol. 35, no. 3, pp. 214-34, Jul, 2013.
[45] M. Fischler, and R. Bolles, "Random sample consensus: a paradigm for model fitting with applications to image analysis and automated cartography," *Communications of the ACM*, vol. 24, no. 6, pp. 381-395, Jun, 1981.
[46] L. Yazdani, M. Bhatt, I. Rafati *et al.*, "The revisited frequency-shift method for shear wave attenuation computation and imaging," *IEEE Transactions on Ultrasonics, Ferroelectrics, and Frequency Control*, vol. 69, no. 6, pp. 2061-2074, 2022.
[47] D. J. Sheskin, *Handbook of parametric and nonparametric statistical procedures*, 5th ed.: CRC Press, 2011.
[48] R. J. Tibshirani, and J. Taylor, "The solution path of the generalized lasso," *The Annals of Statistics*, vol. 39, no. 3, pp. 1335-1371, Jun, 2011.
[49] A. Kolmogorov, "Sulla determinazione empirica di una lgge di distribuzione," *Giornale dell'Istituto Italiano degli Attuari,* vol. 4, pp. 83-91, 1933.
[50] P. M. Shankar, "A general statistical model for ultrasonic backscattering from tissues," *IEEE Transactions on Ultrasonics, Ferroelectrics, and Frequency Control*, vol. 47, no. 3, pp. 727-736, Feb, 2000.
[51] G. Schwartz, "Estimating the dimension of a model," *Annals of Statistics*, vol. 6, pp. 461-464, Mar, 1978.
[52] E. L. Madsen, J. A. Zagzebski, R. A. Banjavie *et al.*, "Tissue mimicking materials for ultrasound phantoms," *Med Phys*, vol. 5, no. 5, pp. 391-394, Sep-Oct, 1978.
[53] D. Garcia, L. Le Tarnec, S. Muth *et al.*, "Stolt's f-k migration for plane wave ultrasound imaging," *IEEE Transactions on Ultrasonics, Ferroelectrics, and Frequency Control* vol. 60, no. 9, pp. 1853-1867, Sep, 2013.
[54] A. Tang, J. Tan, M. Sun *et al.*, "Nonalcoholic fatty liver disease: MR imaging of liver proton density fat fraction to assess hepatic steatosis," *Radiology*, vol. 267, no. 2, pp. 422-31, May, 2013.
[55] A. Tang, A. Desai, G. Hamilton *et al.*, "Accuracy of MR imaging-estimated proton density fat fraction for classification of dichotomized histologic steatosis grades in nonalcoholic fatty liver disease," *Radiology*, vol. 274, no. 2, pp. 416-425, Feb, 2015.
[56] R. P. Carbente, J. M. Maia, and A. A. Assef, "Image reconstruction utilizing median filtering applied to elastography," *BioMedical Engineering OnLine*, vol. 18, no. 1, pp. 22 (31 pages), Mar, 2019.
[57] J. S. Paige, G. S. Bernstein, E. Heba *et al.*, "A pilot comparative study of quantitative ultrasound, conventional ultrasound, and MRI for predicting histology-determined steatosis grade in adult nonalcoholic fatty liver disease," *American Journal of Roentgenology* vol. 208, no. 5, pp. 168-177, May, 2017.
[58] Y. Y. Liao, K. C. Yang, M. J. Lee *et al.*, "Multifeature analysis of an ultrasound quantitative diagnostic index for classifying nonalcoholic fatty liver disease," *Scientific Reports* vol. 6, pp. 35083 (11 pages), Oct, 2016.
[59] T. Tada, H. Iijima, N. Kobayashi *et al.*, "Usefulness of attenuation imaging with an ultrasound scanner for the evaluation of hepatic steatosis," *Ultrasound in Medicine & Biology*, vol. 45, no. 10, pp. 2679-2687, Oct, 2019.
[60] T. Tada, T. Kumada, H. Toyoda *et al.*, "Utility of attenuation coefficient measurement using an ultrasound-guided attenuation parameter for evaluation of hepatic steatosis: comparison with MRI-determined proton density fat fraction," *American Journal of Roentgenology*, vol. 212, no. 2, pp. 332-341, Feb, 2019.
[61] K. Imajo, H. Toyoda, S. Yasuda *et al.*, "Utility of ultrasound-guided attenuation parameter for grading steatosis with reference to MRI-PDFF in a large cohort," *Clinical Gastroenterology and Hepatology*, no. 21, pp. 1182-1184, Nov, 2021.
[62] V. Barrere, M. Sanchez, S. Cambronero *et al.*, "Evaluation of ultrasonic attenuation in primary and secondary human liver tumors and its potential effect on high-intensity focused ultrasound treatment," *Ultrasound in Medicine & Biology*, vol. 47, no. 7, pp. 1761-1774, Jul, 2021.
[63] N. Jafarpisheh, T. J. Hall, H. Rivaz *et al.*, "Analytic global regularized backscatter quantitative ultrasound," *IEEE Transactions on Ultrasonics, Ferroelectrics, and Frequency Control*, vol. 68, no. 5, pp. 1605-1617, 2021.
[64] K. A. Wear, "A Gaussian framework for modeling effects of frequency-dependent attenuation, frequency-dependent scattering, and gating," *IEEE Transactions on Ultrasonics, Ferroelectrics, and Frequency Control*, vol. 49, no. 11, pp. 1572-82, Nov, 2002.
[65] M. Hassannejad Bibalan, and H. Amindavar, "Non-Gaussian amplitude PDF modeling of ultrasound images based on a novel generalized Cauchy-Rayleigh mixture," *EURASIP Journal on Image and Video Processing*, vol. 2016, no. 1, pp. 48, Dec, 2016.
[66] P. Gong, P. Song, C. Huang *et al.*, "Noise suppression for ultrasound attenuation coefficient estimation based on spectrum normalization," *IEEE Transactions on Ultrasonics, Ferroelectrics, and Frequency Control*, vol. 68, no. 8, pp. 2667-2674, Aug, 2021.

Iman Rafati is currently pursuing the Ph.D. degree in biomedical engineering at the Université de Montréal, Montréal, Québec, Canada. He received the bachelor's degree in computational engineering sciences, and master's degree in biomedical engineering from the University of Tehran, Tehran, Iran in 2014 and 2016, respectively. His current research interests are in quantitative ultrasound (QUS) imaging, elastography, and liver cancer diagnosis by QUS.

François Destrempes received the B.Sc. degree in mathematics from the Université de Montréal, Montréal, Québec, Canada, in 1985, the Ph.D. degree in mathematics from Cornell University, Ithaca, NY, USA, in 1990, and the Ph.D. degree in computer science from the University of Montreal, in 2006. Since 2008, he is a Research Assistant with the Laboratory of Biorheology and Medical Ultrasonics, Centre de recherche de l'Université de Montréal, Montréal. Dr. Destrempes has authored or coauthored 45 articles and two book chapters. His current research interests include ultrasound imaging, segmentation of ultrasound images, quantitative ultrasound, and machine learning applied to medical imaging.

Ladan Yazdani received her B.Sc. degree in electrical engineering (minor in biomedical engineering) in 2015, and M.Sc. degree in biomedical engineering in 2018 from University of Tehran, Tehran, Iran. She is currently a Ph.D. candidate in biomedical engineering at the Université de Montréal, Montréal, Québec, Canada. She joined the Laboratory of Biorheology and Medical Ultrasonics, Centre de recherche de l'Université de Montréal, Montréal, Québec, Canada in 2019. Her current research interests include ultrasound imaging, ultrasound elastography, and liver diseases diagnosis by ultrasound.

Marc Gesnik received the Engineering degree from the École Supérieure de Physique et de Chimie Industrielles de la Ville de Paris (ESPCI Paris), Paris, France, in 2014, the M.Sc. degree in physical acoustics from Paris VII University, Paris, in 2014, and the Ph.D. degree from the Institut Langevin, CNRS–INSERM–ESPCI Paris, in 2017. He was a Post-Doctoral Fellow with the Centre de recherche de l'Université de Montréal, Montréal, Québec, Canada. His research interests include elastography, quantitative ultrasound imaging, functional ultrasound imaging, and photoacoustics. He is now working for the Iconeus company in Paris.

An Tang received the M.D. degree from University of Sherbrooke, Canada in 2000 and completed his Radiology residency at the Université de Montréal, Canada in 2005. He pursued fellowship training in abdominal imaging at the University of Toronto, Canada in 2006. He is currently a clinical scientist at the Centre de recherche du Centre hospitalier de l'Université de Montréal, senior research scholar of the Fonds de recherche du Québec — Santé (FRQS), and Professor of Radiology at the Université de Montréal. His research interests focus on imaging-based techniques for diagnosis and monitoring of chronic liver disease and liver cancer.

Guy Cloutier is Director of the Laboratory of Biorheology and Medical Ultrasonics, University of Montreal Hospital Research Center; and Professor at the Department of Radiology, Radiation Oncology, and Nuclear Medicine, and Institute of Biomedical Engineering at Université de Montréal. He has authored more than 230 peer reviewed articles, has several patents, and licensed four technologies. His research interests are in quantitative ultrasound imaging, quasi-static and dynamic ultrasound elastography, development of multi-physics imaging methods, and biomechanical modeling. Dr. Cloutier was a recipient of the National Scientist Award of the Fonds de la Recherche en Santé du Québec.